Published in final edited form as:
Nat Struct Mol Biol. 2015 November ; 22(11): 914–919. doi:10.1038/nsmb.3112.

Mechanism of eIF6 release from the nascent 60S ribosomal subunit

Félix Weis[1,2,3,4], **Emmanuel Giudice**[5], **Mark Churcher**[2,3,4], **Li Jin**[2,3,4,6], **Christine Hilcenko**[1,2,3,4], **Chi C Wong**[7], **David Traynor**[6], **Robert R Kay**[6], and **Alan J Warren**[1,2,3,4]

[1]Cambridge Institute for Medical Research, Cambridge, UK

[2]Medical Research Council Laboratory of Molecular Biology, University of Cambridge Research Unit, Cambridge, UK

[3]Department of Haematology, University of Cambridge, Cambridge, UK

[4]Wellcome Trust–Medical Research Council Stem Cell Institute, University of Cambridge, Cambridge, UK

[5]Université de Rennes 1, Centre Nationale de la Recherche Scientifique, Unité Mixte de Recherche 6290, Institut de Génétique et Développement de Rennes, Rennes, France

[6]Medical Research Council Laboratory of Molecular Biology, Cambridge, UK

[7]Experimental Cancer Genetics, Wellcome Trust Sanger Institute, Cambridge, UK

Abstract

SBDS protein (deficient in the inherited leukemia-predisposition disorder Shwachman-Diamond syndrome) and the GTPase EFL1 (an EF-G homolog) activate nascent 60S ribosomal subunits for translation by catalyzing eviction of the antiassociation factor eIF6 from nascent 60S ribosomal subunits. However, the mechanism is completely unknown. Here, we present cryo-EM structures of human SBDS and SBDS–EFL1 bound to *Dictyostelium discoideum* 60S ribosomal subunits with and without endogenous eIF6. SBDS assesses the integrity of the peptidyl (P) site, bridging uL16 (mutated in T-cell acute lymphoblastic leukemia) with uL11 at the P-stalk base and the sarcin-ricin loop. Upon EFL1 binding, SBDS is repositioned around helix 69, thus facilitating a conformational switch in EFL1 that displaces eIF6 by competing for an overlapping binding site on the 60S ribosomal subunit. Our data reveal the conserved mechanism of eIF6 release, which is corrupted in both inherited and sporadic leukemias.

Correspondence should be addressed to A.J.W. (ajw1000@cam.ac.uk).

Accession codes. The cryo-EM density maps have been deposited in the Electron Microscopy Data Bank under accession codes EMD-3145 (60S–eIF6–SBDS), EMD-3146 (60S–eIF6–SBDS–EFL1) and EMD-3147 (60S–SBDS–EFL1). The corresponding atomic coordinates have been deposited in the Protein Data Bank under accession codes 5AN9, 5ANB and 5ANC, respectively.

Author Contributions

F.W. performed sample preparation, EM data collection, image processing and model refinement. E.G. performed model building and fitting; M.C., L.J. and A.J.W. performed genetic and biochemical experiments; C.H. performed protein expression and purification; C.C.W. generated mutant *Dictyostelium* strains with advice from D.T. and R.R.K.; and D.T. and F.W. cultured *Dictyostelium* cells. F.W. and A.J.W. designed experiments and wrote the manuscript with input from all authors.

Competing Financial Interests

The authors declare no competing financial interests.

Europe PMC Funders Author Manuscripts

Europe PMC Funders Author Manuscripts

The nascent large (60S) ribosomal subunit undergoes an ordered series of final maturation steps in the cytoplasm before it becomes competent to enter translation1. In particular, the Shwachman-Bodian-Diamond syndrome protein (SBDS, Sdo1 in *Saccharomyces cerevisiae*), which is deficient in the inherited leukemia-predisposition disorder Shwachman-Diamond syndrome (SDS)2, cooperates with the GTPase elongation factor–like 1 (EFL1, also known as EFTUD1) in catalyzing eviction of the ribosome antiassociation factor eukaryotic initiation factor 6 (eIF6, Tif6 in *S. cerevisiae*)3–6. The eIF6 protein sterically blocks formation of the B6 intersubunit bridge7,8 by binding to the sarcin-ricin loop (SRL), uL14 and eL24 (unified nomenclature for ribosomal proteins9) on the 60S intersubunit face and must therefore be removed to allow the assembly of actively translating 80S ribosomes10. Upon release, eIF6 shuttles back to the nucleus, where it plays an essential part in the biogenesis and nuclear export of the 60S ribosomal subunit11.

SDS is characterized by poor growth, exocrine pancreatic insufficiency, skeletal abnormalities and bone-marrow failure, with a 30–40% risk of progression to myelodysplastic syndrome and acute myeloid leukemia12. Interestingly, a subset of T-cell acute lymphoblastic leukemias (T-ALLs) are associated with recurrent uL16 mutations13 that impair the release of Tif6 (and the 60S nuclear-export adaptor Nmd3) when expressed in yeast. Together, these data support the hypothesis that defective late maturation of the 60S ribosomal subunit may drive leukemic transformation. However, the mechanistic link between SBDS, uL16 and eIF6 remains unclear.

Like eIF6, the SBDS protein is shared by eukaryotes and archaea. X-ray crystallography and solution NMR spectroscopy have revealed the conserved tripartite architecture of the SBDS protein5,14–16. Human SBDS comprises domains I (FYSH domain, residues S2–S96), II (residues D97–A170) and III (residues H171–E250). EFL1 is homologous to the ribosomal translocase EF-G in prokaryotes and to elongation factor 2 (EF-2) in eukaryotes3. Like EF-2, EFL1 has an overall five-domain architecture, including domain I, which contains the G1–G5 motifs that bind and hydrolyze GTP. Intriguingly, the ferredoxin-like fold of SBDS domain III is most closely related to domain V of EF-2, which is also found in EFL1 (ref. 14). The presence of an insertion of variable length within domain II distinguishes EFL1 from other ribosomal translocases.

To elucidate the mechanism eIF6 release from nascent 60S ribosomal subunits, we used single-particle cryo-EM to determine the structures of native *D. discoideum* pre-60S ribosomal subunits with and without endogenous eIF6 bound to human SBDS and SBDS–EFL1. We show that dynamic rotation of the SBDS protein in the ribosomal P site is coupled to a conformational switch in EFL1 that promotes eIF6 displacement through competition for an overlapping binding site on the 60S ribosomal subunit. Together, our data reveal the mechanism underlying a key conserved quality-control step during 60S-subunit maturation; this step is corrupted in human leukemia-associated ribosomopathies.

Results

SBDS contacts uL16 in the ribosomal P site

To determine the mechanism of eIF6 release, we capitalized on the observation that human SBDS and EFL1 can evict eIF6 from purified native *Dictyostelium* pre-60S subunits6. Using single-particle cryo-EM and *in silico* sorting, we determined the structures of three complexes (60S–eIF6–SBDS, 60S–eIF6–SBDS–EFL1 and 60S–SBDS–EFL1) from a single heterogeneous mixture containing the non-hydrolyzable GTP analog β,γ-methyleneguanosine 5′-triphosphate (GMPPCP), human SBDS and EFL1 and native *Dictyostelium* 60S ribosomal subunits carrying endogenous eIF6. We were able to trap eIF6 on 85% of the native pre-60S subunits by using a *Dictyostelium* strain (HM2917) that overexpresses a dominant-negative SBDS-GFP fusion protein6 (Online Methods). A low concentration of glutaraldehyde was added to reduce preferential particle orientation on the cryo-EM grid.

We generated a 3D cryo-EM map of the 60S–eIF6–SBDS complex at 3.3-Å resolution (Fig. 1a,b and Supplementary Figs. 1 and 2a). Although the local resolution (Supplementary Fig. 2b) extended to 3 Å in some areas of the 60S–eIF6–SBDS complex, thus allowing unambiguous visualization of RNA bases (Supplementary Fig. 2c) or ribosomal protein side chains (Supplementary Fig. 2d), the resolution decreased toward the periphery, particularly for the bound assembly factors. In the 60S–eIF6–SBDS complex, the resolution of the SBDS protein was in the range of 4–5 Å, thus allowing identification of α-helices and β-sheets (Supplementary Fig. 2e). The maps allowed us to fit and refine homology models of *Dictyostelium* eIF6, ribosomal proteins, rRNA fragments and the solution NMR structure of human SBDS5 (Supplementary Figs. 2g,i and 3 and Supplementary Tables 1 and 2).

The structure of the 60S subunit reflects that of the mature ribosome17–19. The eIF6-binding site is conserved, and it involves the C terminus of uL14, which is in proximity to the SRL, the loop formed by residues 58–71 of uL3 and the N terminus of eL24 (refs. 7,8,20) (Fig. 1c). There is no direct contact between eIF6 and SBDS. In agreement with results from *in vitro* binding studies21, SBDS domain I occupies the P site of the 60S ribosomal subunit, packing between the P loop (helix 80), helix 69 and the conserved essential internal loop of uL16, a ribosomal protein that is targeted by recurrent mutations (R98S, R98C and Q123P) in T-ALL13 (Fig. 1d). On one face of the β-hairpin at the base of uL16, residue Q123 (M123 in *Dictyostelium*) lies in proximity to SBDS domain I (helix α2). According to the yeast 80S crystal structure17, the side chain of the highly conserved uL16 residue R98 on the opposite face of the hairpin is likely to make an electrostatic interaction with helix 39 (nucleotides 1363 and 1364). SBDS residues S2–V15 interact with components of the peptidyl transferase center (PTC), the six N-terminal residues extending into the ribosomal peptide-exit tunnel (Fig. 1b). SBDS domain III, like domain V of EF-G22 and EF-2 (ref. 23), contacts the SRL (helix 95) and the P-stalk base (uL11, helices 43 and 44) (Fig. 1e). Thus, SBDS shields the active sites of the 60S subunit including the P site, PTC, the entrance to the polypeptide-exit tunnel and the binding site at the P-stalk base for the translational GTPases. Furthermore, our data reveal a direct structural link on the

ribosome between SBDS (mutated in the inherited leukemia-predisposition disorder SDS) and uL16 (mutated in acquired pediatric T-ALL).

EFL1 and eIF6 compete for an overlapping binding site

Because of the lack of direct contact between SBDS and eIF6, we hypothesized that EFL1, like its homolog EF-2, might bind in the canonical translational GTPase center, where it might potentially interact with both SBDS and eIF6. To test this hypothesis, we obtained cryo-EM maps of complexes containing 60S–eIF6–SBDS–EFL1 (Fig. 2a) and 60S–SBDS–EFL1 (lacking endogenous eIF6) (Fig. 2b) at overall resolutions of 4.1 Å and 4.2 Å, respectively (Supplementary Fig. 2a). The local resolution for EFL1 was in the range of 8–9 Å, thus limiting interpretation to protein domains (Supplementary Fig. 2b,f). In the absence of a high-resolution EFL1 crystal structure, we built a homology model for human EFL1 (Online Methods and Supplementary Fig. 4a–c) and docked this together with SBDS and eIF6 unambiguously into the cryo-EM maps (Supplementary Figs. 2h,i and 4d–g and Supplementary Tables 1 and 2).

EFL1 adopts two distinct conformations. In the 60S–eIF6–SBDS–EFL1 complex, in agreement with results from competitive EF-2 binding assays24, EFL1 binds a site on the intersubunit face of the large subunit that is common to other canonical translational GTPases22,25,26. However, of the total EFL1 buried surface area (4,609.3 $Å^2$), only 13.5% contacts rRNA, and the remainder binds SBDS (33%), eIF6 (40%), uL11 (12%) and uL10 (1.5%). In transition to the 60S–SBDS–EFL1 complex, EFL1 undergoes a large-scale arc-like interdomain movement with domains I and II (~20 Å) and IV (~10 Å) pivoting around the relatively fixed axis formed by domains III and V (Fig. 2c and Supplementary Movie 1). EFL1 undergoes an overall ‘accommodation’ on the 60S subunit that results in more extensive interactions with the rRNA (24% of the total buried surface area of 4,762.4 $Å^2$), ribosomal proteins (34%) and SBDS (42%). By competing with eIF6 for an overlapping binding site on the 60S ribosomal subunit, the accommodated EFL1 conformation is incompatible with simultaneous binding of eIF6 (Fig. 2d). Specifically, in the accommodated state, EFL1 domain I comes into close contact with the tip of the SRL and with uL14 (Fig. 2e,f). Although the EFL1 domain II insertion (that distinguishes EFL1 from EF-2) also contacts eIF6, genetic complementation experiments in *S. cerevisiae* revealed that it was dispensable for EFL1 function *in vivo* (Supplementary Fig. 5a,b). Furthermore, in contrast with results from previous reports27,28, Tif6 residues S174 and S175 (and indeed the poorly conserved C-terminal 21 amino acids) were dispensable for Tif6 recycling *in vivo* (Supplementary Fig. 5c,d). We conclude that in the accommodated conformation, EFL1 domain I has a critical role in competing with eIF6 for the overlapping binding site on the SRL.

Dynamic rotation of SBDS

In agreement with the global domain motions observed by solution NMR spectroscopic analysis5, SBDS domain II undergoes a 60° rotation on EFL1 binding, with a pivot point through the N terminus of helix α5 (Fig. 3a–d and Supplementary Movie 2). SBDS domain III rotates 180° away from the P-stalk base (‘closed’ state) toward helix 69 (‘open’ state) while SBDS domain I remains anchored in the P site. Displacement of SBDS domain III

from its binding site at the P-stalk base by EFL1 domain V explains the intriguing structural homology between these two protein domains of diverse amino acid sequence14: SBDS and EFL1 both share a common binding site on the 60S subunit but cannot bind simultaneously to the P-stalk base.

Interpreting disease-related SBDS variants

Owing to the conservation of rRNA and ribosomal protein sequences between human and *Dictyostelium*, our structure allows us to interpret the consequences of SDS-associated disease mutations in a ribosomal context. We set out to functionally validate the importance of the potential contacts between SBDS and the ribosome observed in our cryo-EM structure by genetic complementation of *SDO1*-deleted (*sdo1*Δ) yeast cells and by analyzing 60S-subunit binding in an *sdo1*Δ suppressor strain (C375) that allows expression of Sdo1 variants as the sole source of Sdo1 (Fig. 4a,b). All three domains were required for Sdo1 function *in vivo*, and domain I was necessary but not sufficient for 60S binding. Several disease-related alleles (*sdo1-F57L*, *sdo1-N67E*, *sdo1-K151N*, *sdo1-K151E* and *sdo1-R224E*) were defective in both the genetic complementation and binding assays. The F57L missense mutation perturbs the fold of SBDS domain I (but not domains II or III)5. The local resolution of the SBDS protein in the maps (4–5 Å) does not allow visualization of individual amino acid side chains. Nevertheless, the structure suggests that the disease-associated residue K67 (yeast N67) in SBDS domain I potentially makes an electrostatic interaction with the P loop (nucleotide G2956) (Fig. 4c). In agreement with this hypothesis, substitution of the *sdo1-N67E* allele with *sdo1-N67G* or *sdo1-N67K* restored both *sdo1*Δ cell growth and Sdo1 binding to the ribosome (Fig. 4a,b). Thus, a specific interaction between Sdo1 domain I and the 60S subunit is required for yeast cell fitness. Upon EFL1 binding, the highly conserved residues K151 (N terminus of helix α7) and R218 (yeast R224, helix α9 of SBDS domain III) potentially make electrostatic interactions with the tip of helix 69 (nucleotides 2522 and 2523) (Fig. 4d). Together with the genetic and biochemical analyses (Fig. 4a,b), our data support a key role for K151 and R218 in stabilizing the open conformation of the SBDS protein. Indeed, because the density for H69 is clear in our maps (the local resolution is 4–5 Å in the 60S–eIF6–SBDS complex), it is reasonable to propose that SBDS stabilizes the conformation of H69, a structural element that is usually not well ordered in isolated 60S subunits. The 60° rotation of SBDS domain II relative to domain I (Fig. 3d) in the presence of EFL1 involves a flexible linker (residues K90–R100) that potentially interacts with the rRNA between helices 69 and 71 (nucleotides 2551 and 2552) (Fig. 4e). The functional importance of the linker is supported by the fitness defects of disease-related alleles (*sdo1-*Δ*94-95* and *sdo1-D97-K98delinsEVQVS*) that alter the linker length and *sdo1-R100E*, which alters the charge of a highly conserved residue at the N terminus of helix α5 (Fig. 4a,b). Flexibility in this region is probably important in facilitating the rotational dynamics of SBDS on the ribosome. We conclude that disease-related SBDS variants target rRNA contacts that are critical for 60S binding and the stabilization of functionally important conformational states. These data provide important *in vivo* validation of the cryo-EM structures.

Interpreting T-ALL–associated uL16 variants

Mutations in uL16 (*uL16-R98S*, *uL16-R98C* and *uL16-H123P*) are recurrently associated with T-ALL and perturb Tif6 (and Nmd3) release in yeast13. Residue R98 of uL16 makes an electrostatic interaction with helix 39 (nucleotides 1363 and 1364) in the crystal structure of the yeast ribosome17. In view of the close interaction in our structure between uL16 and SBDS in the P site (Fig. 1d), we hypothesized that, like *uL16-S104D*21,29, the T-ALL–associated *uL16-R98S* allele might impair Tif6 release indirectly by destabilizing the interaction of uL16 with helix 39, thereby altering the conformation of the uL16 P-site loop and reducing Sdo1 binding *in vivo*. Supporting this hypothesis, the T-ALL alleles *uL16-R98S*, *uL16-R98C* and *uL16-H123P* all impaired yeast cell fitness and 60S binding by Sdo1 *in vivo* (Supplementary Fig. 5e–g). However, unlike *uL16-R98S* and *uL16-R98C*, the *uL16-H123P* allele markedly reduced uL16 protein expression, causing a severe fitness defect (Supplementary Fig. 5e), probably as a consequence of proline-induced unfolding of the uL16 β4-β5 hairpin. We conclude that T-ALL–associated uL16 mutations indirectly impair eIF6 release by reducing SBDS recruitment to nascent 60S subunits *in vivo*.

Discussion

Mechanism of eIF6 release

Our cryo-EM, biochemical and genetic analyses allow us to propose a mechanism for eIF6 release, a key conserved step in the translational activation of ribosomes that is mediated by SBDS and the GTPase EFL1 in eukaryotes and probably by EF-2 in archaea (Fig. 5a–d and Supplementary Movie 3). We propose a cofactor-dependent conformational-switching model30 in which EFL1 initially binds to the GTPase center, in direct contact with SBDS and eIF6, in a low-affinity, inactive GTP-bound state (Fig. 5b). Competing with SBDS for an overlapping binding site, EFL1 domain V promotes a 180° rotational displacement of SBDS domain III away from the P-stalk base (closed state) toward helix 69 (open state), causing the SBDS protein to adopt a conformation that is probably stabilized by interactions between SBDS residues K151 and R218 and helix 69 (Figs. 3a–d and 4d). We suggest that in the open state, SBDS drives the equilibrium of GTP-bound EFL1 toward an active high-affinity (‘accommodated’) SRL-bound conformation that effectively competes with eIF6 for an overlapping binding site on the SRL and promotes eIF6 displacement from the 60S subunit (Fig. 5c). In the final step of the catalytic cycle (Fig. 5d), we propose that the interaction of EFL1 with the SRL promotes GTP hydrolysis, thereby shifting the EFL1 conformational equilibrium from a high- to a low-affinity ribosome binding state and promoting dissociation of both EFL1 and SBDS from the 60S subunit. However, further work is required to determine the precise timing and role of GTP hydrolysis in the mechanism of eIF6 release. It is conceivable that glutaraldehyde may have trapped the less-populated accommodated EFL1 state on 60S subunits lacking eIF6 (15% of the initial purified population). Nevertheless, we propose that the SRL-bound accommodated EFL1 state defines a functionally relevant conformation because it clearly overlaps with the eIF6-binding site. In agreement with this hypothesis, clusters of mutations in yeast EFL1 that suppress the P-site-loop mutant *uL16-S104D* map to domain interfaces that are involved in the conformational change that EF-2 and EF-G undergo during translocation29. We hypothesize that such mutations may drive the EFL1 conformational equilibrium toward the accommodated state.

SBDS has been proposed as a tRNA mimic16 that is driven into the P site by EFL1 in a pseudotranslocation event21,29. However, in the absence of EFL1, SBDS binds to the 60S subunit in an extended orientation that differs completely from any orientations previously observed for tRNA (Fig. 1a). We suggest that the structural mechanism of eIF6 eviction is more reminiscent of bacterial ribosome recycling by RRF and EF-G31–35 (Fig. 5e–h). SBDS binds in the 60S-subunit interface cavity in an orientation that is remarkably similar to that of RRF on the bacterial 50S subunit (Fig. 5f), and SBDS and RRF undergo similar extensive interdomain rotations on the large ribosomal subunit in the presence of their respective cooperating GTPases (Fig. 5g,h). SBDS is a multitasking protein: domain I protects and potentially proofreads the peptide-exit tunnel and PTC; domain II promotes EFL1 conformational switching and, together with domain I, mediates 60S binding and dynamic interdomain motion; domain III first shields the translational GTPase-binding site at the P-stalk base and later, in the open conformation, promotes EFL1 conformational switching.

Final quality-control assessment of the nascent 60S subunit

As the substrate for our cryo-EM studies, we used late pre-60S particles purified from *Dictyostelium* cells overexpressing a dominant-negative SBDS mutant6. The structure of these pre-60S particles reflects that of a mature 60S subunit,17–19 enriched in bound eIF6 (but not Nmd3) and with uL16 already integrated. Loading of uL16 is critical for Nmd3 eviction36 and for Sdo1 binding to the 60S subunit *in vivo* (Supplementary Fig. 5f,g). Together, these data support the hypothesis that SBDS is recruited to an eIF6-bound pre-60S particle after uL16 loading and Nmd3 removal (Fig. 5a) and place release of eIF6 (rather than Nmd3 (ref. 1)) as the final step in 60S-subunit maturation.

Because eIF6 sterically blocks ribosomal-subunit joining8, its eviction licenses the entry of mature 60S subunits into the actively translating pool. We propose that by ‘proofreading’ the peptide-exit tunnel, the P site and the GTPase center, SBDS and EFL1 both have key roles in coupling eIF6 release to a final quality-control assessment of the integrity of the active sites of the 60S subunit. Similarly, the maturing 40S subunit is subject to a final proofreading step37,38. Together with the structures of 60S–eIF6 (refs. 7,8,20), 60S–Nmd3 (ref. 39) and 60S–Arx1 (refs. 40,41) complexes, our data strengthen the hypothesis that cytoplasmic pre-60S assembly factors have critical roles in structural proofreading and preventing premature translation by masking the active sites of the ribosome. The intriguing presence of a rod-shaped density in the polypeptide-exit tunnel in the 60S–Arx1–Rei1 complex suggests that the tunnel itself is subjected to proofreading40. The presence of six N-terminal residues of the SBDS protein in the proximal part of the polypeptide-exit tunnel (Fig. 1b,d) reinforces this concept and raises the possibility that the entire length of the tunnel may undergo proofreading during assembly. Finally, the competition between EFL1 and eIF6 for an overlapping binding site on the SRL provides an elegant mechanism to couple a quality-control assessment of the functional integrity of the SRL to the last step in the EFL1 catalytic cycle (GTP hydrolysis).

The oncogenic ribosome

Our data reveal an allosteric cascade in which large-scale dynamic movements in SBDS and EFL1 link the conserved P-site loop of uL16 with eIF6. Our study links the pathogenesis of inherited (SDS) and sporadic (T-ALL) forms of leukemia in a common pathway involved in 60S-subunit maturation and the translational activation of ribosomes. Interestingly, SBDS deficiency appears to promote acquired interstitial deletions of chromosome 20, which encompass the *EIF6* gene, in bone-marrow cells of individuals with SDS42, thus providing a potential mechanism to suppress the defect in ribosome biogenesis by reducing the copy number of the *EIF6* gene. However, precisely how defective late-60S ribosomal-subunit maturation promotes the multistep progression to myelodysplastic syndrome and leukemia and the effects of compensatory suppressor mutations in this process remain key unanswered questions.

In conclusion, our study illustrates the power of cryo-EM and *in silico* sorting of a single heterogeneous population to illuminate the mechanism underlying a dynamic and fundamental late step in 60S-subunit maturation that is corrupted in the human ribosomopathies SDS and T-ALL.

Online Methods

Yeast strains and plasmids

S. cerevisiae strains used in this study are listed in Supplementary Table 3, and the plasmids and primers are listed in Supplementary Tables 4 and 5, respectively. Mutations were generated by QuikChange site-directed mutagenesis (Stratagene). For 60S binding assays, a 3×FLAG cassette was inserted at the 3′ end of the *SDO1* coding sequence (Supplementary Table 5).

Genetic complementation assays

For random sporulation assays, double-mutant *tif6*Δ::*KanMX4 sdo1*Δ::*NatMX4* cells (strain AJW3) were transformed with empty vector (pRS316) as a control or plasmids expressing wild-type *TIF6* or *TIF6* mutants. Similarly, double-mutant *efl1*Δ::*KanMX4 sdo1*Δ::*NatMX4* cells (strain SE1) were transformed with empty vector (pRS316) or plasmid pAJW2 (expressing the *EFL1*Δ*420-580* mutant). Diploid cells were sporulated and cultured on solid –Ura medium, which selects for the germination of *MAT***a** meiotic progeny carrying the indicated plasmids and contained 200 mg/mL G418 to select for *tif6*Δ::*KanMX4* or *efl1*Δ::*KanMX4* cells. Plates were incubated for 4 d at 30 °C. Viable single colonies were spotted in ten-fold serial dilutions onto solid –Ura medium for 3 d at 30 °C. Conditional haploid (strain H1) cells (*sdo1*Δ::*KanMX4*/*pYC2*[*GAL10*::*SDO1*]) were transformed with plasmids (*CEN, LEU*) expressing wild-type or variant *SDO1-3×FLAG* and plated onto solid medium containing 5-fluoroorotic acid (1 mg/mL) counterselection for 3–5 d at 30 °C. For 60S binding assays, FLAG-tagged Sdo1 variants were expressed as the sole source of Sdo1 in *sdo1*Δ cells containing a gain-of-function *TIF6* suppressor allele (strain C375, *sdo1*Δ *TIF6-I58T* cells) to maintain fitness. FLAG-tagged Sdo1 variants were visualized by immunoblotting with anti-FLAG antiserum (Sigma, A8592).

Mutant uL16 proteins were visualized by immunoblotting of extracts from strains SP103, SP106 and SP107 (Supplementary Table 3) after repression of endogenous uL16 (Rpl10) by the addition of glucose for 16 h. For 60S binding studies, cells were transformed with plasmids (*CEN, URA*) expressing wild-type *SDO1-3×FLAG*. Anti-uL14 (Rpl23) antibody was obtained from Abcam (112587). Anti-uL16 (Rpl10) rabbit polyclonal antiserum was a kind gift from B. Trumpower (Dartmouth Medical School)4. Original images of blots used in this study can be found in Supplementary Data Set 1.

Preparation of yeast extracts

Log-phase yeast cell pellets stored at −80 °C were thawed slowly in 1 mL of ice-cold polysome lysis buffer (10 mM Tris-HCl, pH 7.4, 50 mM NaCl, 1 mM DTT, 5 mM MgCl2, and 0.1 mg/mL cycloheximide) with protease inhibitors (Roche) added according to the manufacturer's instructions. Cells were ribolyzed (Powerlyser-24, MoBio) at 3 × 3,500 m/s for 45 s, and samples were cleared twice in a chilled microcentrifuge (Eppendorf) at 13,000 r.p.m. for 10 min. The clarified supernatant was divided into aliquots and stored at −80 °C.

Sucrose cushions

50 µL yeast extracts (5–10 OD_{260}) was layered onto a 50-µL 1.1 M sucrose cushion (1.1 M sucrose, 50 mM Tris-HCl, pH 7.4, 1 mM DTT, and NaCl ranging from 0 to 150 mM). Samples were centrifuged (Beckmann TLA100 rotor) at 100,000 r.p.m. for 90 min at 4 °C. The supernatant (including the cushion volume) was placed in a fresh tube, and 25 µL 4× protein loading dye (4× LDS Novex/Invitrogen) was added. The pellet was resuspended in 125 µL 1× loading dye. After heating for 5 min at 90 °C, 15 µL of sample was electrophoresed in a 4–12% Novex gel in MES buffer for 50 min at 200 V and immunoblotted.

SDO1 suppressor mutations

PCR was used to amplify the coding sequence for wild-type *SDO1* plus 500 bp 5′ and 3′ of the open reading frame from yeast genomic DNA. The PCR product was cloned into the vector pRS314 (*CEN, TRP*). An identical restriction site (AatII) was introduced immediately 5′ and 3′ of the *SDO1* open reading frame. The *SDO1* plasmid was liberated and the plasmid religated ('acceptor' plasmid). Error-prone PCR (GenemorphII, Agilent Technologies) was used to mutagenize *SDO1* with primers with 50 bp of complementary sequence 5′ and 3′ of the *SDO1* open reading frame. The PCR product and the linearized (with AatII) acceptor plasmid were transformed into the appropriate yeast strain, and suppressors were selected by plating onto selective media.

Purification of *Dictyostelium* 60S ribosomal subunits carrying eIF6

Dictyostelium cells (strain HM2917 (ref. 6)) were grown axenically in HL5 medium plus glucose (Formedia) in shaking suspension at 22 °C to ~1.4×10^6 cells/mL and treated with cycloheximide (0.1 mg/mL) (Sigma-Aldrich) for 5 min before harvesting by centrifugation. Cells were washed once in KK2 buffer (16.5 mM KH_2PO_4, 3.9 mM K_2HPO_4, 2 mM $MgSO_4$ and 0.1 mM $CaCl_2$) with 0.1 mg/mL cycloheximide, and cell pellets were flash cooled in

liquid nitrogen and stored at −80 °C. To maintain the native eIF6 complex, mild salt conditions (100 mM $K(CH_3COO)$ and 10 mM $Mg(CH_3COO)_2$) were used in all the steps.

Cells were resuspended in lysis buffer (50 mM HEPES-KOH, pH 7.5, 100 mM $K(CH_3COO)$, 10 mM $Mg(CH_3COO)_2$, 6 mM β-mercaptoethanol, 10% (v/v) glycerol, EDTA-free protease inhibitors (Roche), 1 mM AEBSF (Melford Laboratories) and 0.1 mg/mL cycloheximide) at ~5×10^8 cells/mL and lysed by passing once through a 5-μm Isopore membrane filter (Millipore). The lysate was cleared by centrifugation at 16,100*g* for 15 min at 4 °C, and ~300 μL was loaded onto a 3.75-mL 10–50% (w/v) sucrose gradient in buffer A (50 mM HEPES-KOH, pH 7.5, 100 mM $K(CH_3COO)$, 10 mM $Mg(CH_3COO)_2$ and 6 mM β-mercaptoethanol) in Polyallomer 11 × 60 mm centrifuge tubes (Beckman Coulter). After centrifugation (Beckman Coulter SW60Ti rotor) at 485,050*g* for 60 min at 4 °C, gradients were fractionated with a Brandel gradient fractionator with continuous UV monitoring (UV-1, Pharmacia) at A_{254nm}, and 60S ribosomal subunit fractions were collected. 500 μL of the 60S ribosomal subunit fraction was loaded onto a 500-μL 35% (w/v) sucrose cushion in buffer A in Thickwall Polycarbonate 11 × 34 mm tubes (Beckman Coulter) and centrifuged (Beckman Coulter TLA-120.2 rotor) at 627,379*g* for 15 min at 4 °C. 60S-subunit pellets were resuspended in buffer A to ~0.4 μM, stored on ice and used immediately.

Preparation of ribosomal complexes for cryo-electron microscopy analysis

Recombinant human SBDS (NP_057122) and EFL1 (NP_078856) were expressed in *E. coli* and *S. cerevisiae* (strain BCY123, provided by A. Newman), respectively and purified as previously described5. Complexes were obtained by mixture of 120 nM purified *Dictyostelium* 60S ribosomal subunits (85% of which carried endogenous *Dictyostelium* eIF6) with 1.2 μM human SBDS and 1.2 μM human EFL1 in the presence of 0.2 mM GMPPCP (Sigma-Aldrich) for 15 min at room temperature, before addition of 0.5% (v/v) glutaraldehyde (Sigma-Aldrich) and incubation for 10 min at 4 °C. Complexes were used immediately for cryo-EM grid preparation. Preliminary cryo-EM studies performed in the absence of glutaraldehyde revealed dramatic preferential orientation of the ribosomal particles on the cryo-EM grid. The resulting 3D reconstruction was distorted and showed artifacts, thus preventing further interpretation.

Electron microscopy

3-μL aliquots of the complexes were applied on glow-discharged holey carbon grids (Quantifoil R2/2). Grids were blotted and flash frozen in liquid ethane with a Vitrobot automat (FEI). Data acquisition was performed under low-dose conditions on a Titan KRIOS microscope (FEI) operated at 300 kV. The data set was recorded on a back-thinned Falcon II detector (FEI) at a calibrated magnification of ×105,263 (resulting in a pixel size of 1.33 Å on the object scale) with a defocus range of 2–3 μm. An in house–built system was used to intercept the videos from the detector at a speed of 16 frames for the 1-s exposures45. Data were acquired automatically with the EPU software (FEI) over two 24-h sessions with two cryo-EM grids generated from the same preparation of ribosomal complexes.

Image processing

Electron micrographs showing signs of drift or astigmatism were discarded, thus resulting in a data set of 3,844 images. 170,581 particles were selected semiautomatically with e2boxer from EMAN2 (ref. 46). Contrast transfer–function parameters were determined with CTFFIND3 (ref. 47). All 2D and 3D classifications and refinements were performed with RELION48,49.

Reference-free 2D classification was used to discard 80S ribosomes and defective particles, thus resulting in a data set of 121,751 particles selected for further analysis (Supplementary Fig. 1). An initial refinement procedure with a 60-Å low-pass-filtered empty *Dictyostelium* 60S ribosomal subunit resulted in an initial cryo-EM reconstruction with an overall resolution of 3.8 Å, revealing a complete 60S ribosomal subunit with additional densities on the intersubunit face, especially in the P site and around the GTPase center.

However, the map suggested heterogeneity in the stoichiometry and/or conformation of the bound factors. Because the refinement was dominated by the 60S subunit, we sorted the images into subsets by a succession of 3D classifications with three masks delimiting areas of interest on the ribosome50,51. The masks were spheres or combinations of spheres with a voxel value of one inside and zero outside, and a soft drop-off of two pixels. Because EFL1 is an EF-2 homolog, the initial mask was applied around the EF-2–binding site on the 60S subunit, and the particles were sorted into six classes (A1–6). Classes A5 and A6 (~16,000 and ~12,000 particles, respectively) showed clear density for EFL1 in two distinct conformations and were processed separately. After 3D refinement, class A6 contained densities corresponding to a 60S–eIF6–SBDS–EFL1 complex. Because class A5 showed heterogeneity around the eIF6-binding site, a second mask was applied to the area encompassing eIF6 and part of EFL1 domain II, and particles were sorted into four classes (B1–4). 3D refinement of the main class (B3, ~10,000 particles) yielded a map of the 60S–SBDS–EFL1 complex. The maps obtained from classes lacking EFL1 (A1 to A4, ~94,000 particles) showed clear density for eIF6 and additional partial densities in the ribosomal P site and P-stalk base. In agreement with results from a preliminary study in which purified recombinant SBDS protein alone was incubated with 60S ribosomal subunits, the latter densities were ascribed to SBDS. A third mask was applied in this area, and particles were sorted into six classes (C1–6). 3D refinement of the main class (C4, ~43,000 particles) yielded a map of the 60S–eIF6–SBDS complex.

To further increase the resolution of the three classes, statistical movie processing was performed as previously described45. Reported overall resolutions (3.3 Å for the 60S–eIF6–SBDS complex, 4.1 Å for the 60S–eIF6–SBDS–EFL1 complex and 4.2 Å for the 60S–SBDS–EFL1 complex) were calculated with the gold-standard FSC = 0.143 criterion52 and were corrected for the effects of a soft mask on the FSC curve with high-resolution noise substitution53 (Supplementary Fig. 2a). The final density maps were corrected for the modulation transfer function of the detector and sharpened by applying a negative B factor that was estimated with automated procedures54.

Modeling of ribosomal RNA fragments

Dictyostelium 26S rRNA (GenBank FR733594.1) was aligned against the sequences of *Tetrahymena thermophila* (GenBank JN547815.1) and *S. cerevisiae* (GenBank JQ277730.1) 26S rRNAs with ClustalW2 (ref. 55). According to the sequence alignment, we chose the crystal structure of the *T. thermophila* 60S ribosomal subunit in complex with initiation factor 6 (PDB 4A18)8 as a template, except for the L1 stalk region (H76, H77, H78, and a portion of H76), for which the *S. cerevisiae* ribosome structure (PDB 3U5H)17 was used. The homology model of the rRNA fragments (A1221–A1270, C1356–C1602, A2392–U2700 and A2925–C3480; Supplementary Fig. 3a) surrounding the SBDS-binding site was constructed with both Assemble2 (ref. 56) and Coot57.

Protein modeling

The human SBDS atomic coordinates were taken from PDB 2L9N5. The sequence of *Dictyostelium* ribosomal proteins uL3 (L3), uL6 (L9), uL10 (P0), uL11 (L12), uL14 (L23), uL16 (L10), eL24 (L24), and eL40 (L40) were retrieved from the Ribosomal Protein Gene Database (http://ribosome.med.miyazaki-u.ac.jp/), and *Dictyostelium* eIF6 and the human EFL1 sequences were retrieved from the NCBI Protein database (http://www.ncbi.nlm.nih.gov/protein/). All the proteins were modeled by homology with the I-TASSER server58,59. In each case, the model with the best C score was selected to build the final structure (Supplementary Table 6). The lower score obtained for the EFL1 model can be explained by the size of the protein and the presence of both a large insertion domain (compared with EF-2 and EF-G) and numerous loop regions that were modeled *ab initio* by the I-TASSER server.

Model building

To build the initial model of the 60S–eIF6–SBDS complex, we used UCSF Chimera60 to rigid-body dock the *T. thermophila* 60S ribosomal subunit in complex with initiation factor 6 (PDB 4A18)8 into the 60S–eIF6–SBDS complex cryo-EM density map. Taking advantage of the high sequence similarity between the two organisms, we used this structure as our reference to align the *Dictyostelium* ribosomal RNA fragments and the uL3, uL6, uL10, uL11, uL14, uL16, eL24, eL40 and eIF6 proteins with Chimera's MatchMaker tool. In a final step, the human SBDS structure was rigid-body fitted into the cryo-EM density map. We used a similar approach to build the 60S–eIF6–SBDS–EFL1 model with the refined 60S–eIF6–SBDS atomic model as the starting conformation and rigid-body fitting the human EFL1 homology model into the cryo-EM density maps.The 60S–SBDS–EFL1 was built in a similar fashion, with the refined 60S–eIF6–SBDS–EFL1 atomic model (without eIF6) as the starting conformation.

Model fitting and refinement

Because of the intermediate resolution of the bound factors, we first used molecular dynamic flexible fitting (MDFF) to fit the NMR structure of human SBDS (PDB 2L9N)5 or homology models for EFL1, eIF6 and the ribosome. For optimal fitting of the models into the EM density map, we used REFMAC v5.8 adapted for EM refinement61.

The initial system was prepared with VMD62. To preserve the secondary structure of the proteins, the Ψ and φ dihedral angles of the amino acid residues in α-helices or β-sheets were harmonically restrained with a force constant of 200 kcal mol^{-1} rad^{-2}. The hydrogen bonds involving backbone atoms from the same residues were maintained through the MDFF procedure63. For this, we used a force constant of 50 kcal mol^{-1} $Å^{-2}$ to restrain the distance between the acceptor and the hydrogen atom, and a force constant of 50 kcal mol^{-1} rad^{-2} to maintain the angle formed by the donor, the hydrogen, and its acceptor. We also restrained the *cis* peptides in their current configurations with a force constant of 200 kcal mol^{-1} rad^{-2} and the chiral centers to their current handedness with a force constant of 50 kcal mol^{-1} rad^{-2}. In the same way, the helical parts of the rRNA were preserved with two 200 kcal mol^{-1} $Å^{-2}$ restraints to maintain the distance between paired bases and a set of 200 kcal mol^{-1} rad^{-2} restraints to maintain the dihedral angles.

The model was optimized by MDFF *in vacuo* with NAMD64, the CHARMM22 CMAP-corrected parameters65 for the protein, the CHARMM27 parameters for the nucleic acids66, and a 0.3 kcal/mol scaling factor to adjust the influence of the cryo-EM map on the model. A multiple time-step integration scheme was used to calculate bonded interactions every femtosecond and nonbonded interactions every two femtoseconds. A cutoff distance of 10 Å was used for the nonbonded interactions. A dielectric constant of 80 was applied to adjust electrostatic interactions, and the temperature was maintained with a Langevin thermostat with a damping coefficient of 5 ps^{-1}.

To optimize fitting of the less well-defined elements of our model, the MDFF procedure was performed with a multistep protocol. First, we performed 10,000 steps of minimization followed by a slow heating to 300 K over the course of 20,000 simulation steps and then performed 1 ns of molecular dynamic (MD) simulation, all while holding the ribosomal RNA fragments and proteins fixed. This allowed the SBDS fitting to improve while maintaining the position of the other components of our model that were already well placed in the cryo-EM density map. We repeated this procedure twice (10,000 steps of minimization, 20,000 steps of thermalization, and 1 ns of MD), freeing first the ribosomal proteins and then the whole system. To improve the overall quality of the 60S–eIF6–SBDS atomic model, we finished by performing 1,000 steps of minimization.

A similar protocol was used for the 60S–eIF6–SBDS–EFL1 and 60S–SBDS–EFL1 models. However, because the optimization protocol was performed in a cascade (in which the MDFF-refined 60S–eIF6–SBDS atomic model was used as the starting conformation to build the 60S–eIF6–SBDS–EFL1 model, and the resulting structure was used as the starting conformation for the 60S–SBDS–EFL1 model), only three steps were necessary because the ribosomal RNA fragments and proteins were for the most part already well fitted in the electron density map. We performed 10,000 steps of minimization, a slow heating to 300 K over the course of 20,000 simulation steps, and 1 ns of MD simulation to optimize the fitting of EFL1, all while holding the rest of the system fixed. We repeated this procedure, this time allowing the entire system to adjust into the cryo-EM density map. We used 1,000 steps of minimization to improve the quality of the atomic models.

Masked areas of the cryo-EM density maps into which the models had been built were used for refinement in REFMAC v5.8 (ref. 61). $FSC_{average}$ was monitored during refinement to follow the fit to density, and the final models were validated with MolProbity (Supplementary Table 1)67. For cross-validation against overfitting, the atoms of our final models were randomly displaced (with an r.m.s. deviation of 0.5 Å), and a refinement procedure was performed against the maps that were reconstructed from only one of the two independent halves of the data used in our gold-standard FSC procedure. FSC curves were calculated between the resulting models and the half maps against which they had been refined (FSC_{work}) as well as the FSC curve between those models and the other half maps (FSC_{test}). The absence of overfitting of the models is demonstrated by the observation that the FSC_{work} and FSC_{test} curves nearly overlap (Supplementary Fig. 2g–i).Contact analysis was performed with VMD62 and the Protein, Interfaces, Surfaces and Assemblies service at the European Bioinformatics Institute (http://www.ebi.ac.uk/pdbe/prot_int/pistart.html)68. UCSF Chimera was used for visual analysis and creating figures and movies60.

Supplementary Material

Refer to Web version on PubMed Central for supplementary material.

Acknowledgments

We thank A. Johnson (University of Texas) and A. Newman (Medical Research Council Laboratory of Molecular Biology) for yeast strains; B. Trumpower (Dartmouth Medical School) for providing uL16 antiserum; S. Chen, C. Savva, S. De Carlo, S. Welsch, F. De Haas, M. Vos and K. Sader for technical support with cryo-EM; G. McMullan for help with movie data acquisition; T. Darling and J. Grimmett for help with computing; A. Brown for help with refinement; and S. Scheres for discussion. This work was supported by a Federation of European Biochemical Societies Long Term Fellowship (to F.W.), the Specialist Programme from Bloodwise (12048 to A.J.W.), the UK Medical Research Council (MRC) (MC_U105161083 to A.J.W. and U105115237 to R.R.K.), a Wellcome Trust strategic award to the Cambridge Institute for Medical Research (100140), a core support grant from the Wellcome Trust and MRC to the Wellcome Trust–Medical Research Council Cambridge Stem Cell Institute, the Tesni Parry Trust (to A.J.W.), Ted's Gang (to A.J.W.) and the Cambridge National Institute for Health Research Biomedical Research Centre.

References

1. Lo KY, et al. Defining the pathway of cytoplasmic maturation of the 60S ribosomal subunit. Mol Cell. 2010; 39:196–208. [PubMed: 20670889]
2. Boocock GR, et al. Mutations in SBDS are associated with Shwachman-Diamond syndrome. Nat Genet. 2003; 33:97–101. [PubMed: 12496757]
3. Senger B, et al. The nucle(ol)ar Tif6p and Efl1p are required for a late cytoplasmic step of ribosome synthesis. Mol Cell. 2001; 8:1363–1373. [PubMed: 11779510]
4. Menne TF, et al. The Shwachman-Bodian-Diamond syndrome protein mediates translational activation of ribosomes in yeast. Nat Genet. 2007; 39:486–495. [PubMed: 17353896]
5. Finch AJ, et al. Uncoupling of GTP hydrolysis from eIF6 release on the ribosome causes Shwachman-Diamond syndrome. Genes Dev. 2011; 25:917–929. [PubMed: 21536732]
6. Wong CC, Traynor D, Basse N, Kay RR, Warren AJ. Defective ribosome assembly in Shwachman-Diamond syndrome. Blood. 2011; 118:4305–4312. [PubMed: 21803848]
7. Gartmann M, et al. Mechanism of eIF6-mediated inhibition of ribosomal subunit joining. J Biol Chem. 2010; 285:14848–14851. [PubMed: 20356839]
8. Klinge S, Voigts-Hoffmann F, Leibundgut M, Arpagaus S, Ban N. Crystal structure of the eukaryotic 60S ribosomal subunit in complex with initiation factor 6. Science. 2011; 334:941–948. [PubMed: 22052974]

Europe PMC Funders Author Manuscripts

9. Ban N, et al. A new system for naming ribosomal proteins. Curr Opin Struct Biol. 2014; 24:165–169. [PubMed: 24524803]
10. Ceci M, et al. Release of eIF6 (p27BBP) from the 60S subunit allows 80S ribosome assembly. Nature. 2003; 426:579–584. [PubMed: 14654845]
11. Basu U, Si K, Warner JR, Maitra U. The *Saccharomyces cerevisiae* TIF6 gene encoding translation initiation factor 6 is required for 60S ribosomal subunit biogenesis. Mol Cell Biol. 2001; 21:1453–1462. [PubMed: 11238882]
12. Donadieu J, et al. Analysis of risk factors for myelodysplasias, leukemias and death from infection among patients with congenital neutropenia: experience of the French Severe Chronic Neutropenia Study Group. Haematologica. 2005; 90:45–53. [PubMed: 15642668]
13. De Keersmaecker K, et al. Exome sequencing identifies mutation in CNOT3 and ribosomal genes RPL5 and RPL10 in T-cell acute lymphoblastic leukemia. Nat Genet. 2013; 45:186–190. [PubMed: 23263491]
14. Shammas C, et al. Structural and mutational analysis of the SBDS protein family: insight into the leukemia-associated Shwachman-Diamond Syndrome. J Biol Chem. 2005; 280:19221–19229. [PubMed: 15701631]
15. Savchenko A, et al. The Shwachman-Bodian-Diamond syndrome protein family is involved in RNA metabolism. J Biol Chem. 2005; 280:19213–19220. [PubMed: 15701634]
16. Ng CL, et al. Conformational flexibility and molecular interactions of an archaeal homologue of the Shwachman-Bodian-Diamond syndrome protein. BMC Struct Biol. 2009; 9:32. [PubMed: 19454024]
17. Ben-Shem A, et al. The structure of the eukaryotic ribosome at 3.0 A resolution. Science. 2011; 334:1524–1529. [PubMed: 22096102]
18. Voorhees RM, Fernandez IS, Scheres SH, Hegde RS. Structure of the mammalian ribosome-Sec61 complex to 3.4 A resolution. Cell. 2014; 157:1632–1643. [PubMed: 24930395]
19. Khatter H, Myasnikov AG, Natchiar SK, Klaholz BP. Structure of the human 80S ribosome. Nature. 2015; 520:640–645. [PubMed: 25901680]
20. Greber BJ, et al. Cryo-EM structure of the archaeal 50S ribosomal subunit in complex with initiation factor 6 and implications for ribosome evolution. J Mol Biol. 2012; 418:145–160. [PubMed: 22306461]
21. Sulima SO, et al. Eukaryotic rpL10 drives ribosomal rotation. Nucleic Acids Res. 2014; 42:2049–2063. [PubMed: 24214990]
22. Gao YG, et al. The structure of the ribosome with elongation factor G trapped in the posttranslocational state. Science. 2009; 326:694–699. [PubMed: 19833919]
23. Anger AM, et al. Structures of the human and *Drosophila* 80S ribosome. Nature. 2013; 497:80–85. [PubMed: 23636399]
24. Graindorge JS, et al. Deletion of EFL1 results in heterogeneity of the 60 S GTPase-associated rRNA conformation. J Mol Biol. 2005; 352:355–369. [PubMed: 16095611]
25. Schmeing TM, et al. The crystal structure of the ribosome bound to EF-Tu and aminoacyl-tRNA. Science. 2009; 326:688–694. [PubMed: 19833920]
26. Becker T, et al. Structure of the no-go mRNA decay complex Dom34-Hbs1 bound to a stalled 80S ribosome. Nat Struct Mol Biol. 2011; 18:715–720. [PubMed: 21623367]
27. Basu U, Si K, Deng H, Maitra U. Phosphorylation of mammalian eukaryotic translation initiation factor 6 and its *Saccharomyces cerevisiae* homologue Tif6p: evidence that phosphorylation of Tif6p regulates its nucleocytoplasmic distribution and is required for yeast cell growth. Mol Cell Biol. 2003; 23:6187–6199. [PubMed: 12917340]
28. Ray P, et al. The *Saccharomyces cerevisiae* 60 S ribosome biogenesis factor Tif6p is regulated by Hrr25p-mediated phosphorylation. J Biol Chem. 2008; 283:9681–9691. [PubMed: 18256024]
29. Bussiere C, Hashem Y, Arora S, Frank J, Johnson AW. Integrity of the P-site is probed during maturation of the 60S ribosomal subunit. J Cell Biol. 2012; 197:747–759. [PubMed: 22689654]
30. Hauryliuk V, Hansson S, Ehrenberg M. Cofactor dependent conformational switching of GTPases. Biophys J. 2008; 95:1704–1715. [PubMed: 18502805]

31. Lancaster L, Kiel MC, Kaji A, Noller HF. Orientation of ribosome recycling factor in the ribosome from directed hydroxyl radical probing. Cell. 2002; 111:129–140. [PubMed: 12372306]
32. Wilson DN, et al. X-ray crystallography study on ribosome recycling: the mechanism of binding and action of RRF on the 50S ribosomal subunit. EMBO J. 2005; 24:251–260. [PubMed: 15616575]
33. Gao N, Zavialov AV, Ehrenberg M, Frank J. Specific interaction between EF-G and RRF and its implication for GTP-dependent ribosome splitting into subunits. J Mol Biol. 2007; 374:1345–1358. [PubMed: 17996252]
34. Weixlbaumer A, et al. Crystal structure of the ribosome recycling factor bound to the ribosome. Nat Struct Mol Biol. 2007; 14:733–737. [PubMed: 17660830]
35. Seshadri A, Singh NS, Varshney U. Recycling of the posttermination complexes of *Mycobacterium smegmatis* and *Escherichia coli* ribosomes using heterologous factors. J Mol Biol. 2010; 401:854–865. [PubMed: 20561528]
36. Hedges J, West M, Johnson AW. Release of the export adapter, Nmd3p, from the 60S ribosomal subunit requires Rpl10p and the cytoplasmic GTPase Lsg1p. EMBO J. 2005; 24:567–579. [PubMed: 15660131]
37. Strunk BS, Novak MN, Young CL, Karbstein K. A translation-like cycle is a quality control checkpoint for maturing 40S ribosome subunits. Cell. 2012; 150:111–121. [PubMed: 22770215]
38. Lebaron S, et al. Proofreading of pre-40S ribosome maturation by a translation initiation factor and 60S subunits. Nat Struct Mol Biol. 2012; 19:744–753. [PubMed: 22751017]
39. Sengupta J, et al. Characterization of the nuclear export adaptor protein Nmd3 in association with the 60S ribosomal subunit. J Cell Biol. 2010; 189:1079–1086. [PubMed: 20584915]
40. Greber BJ, Boehringer D, Montellese C, Ban N. Cryo-EM structures of Arx1 and maturation factors Rei1 and Jjj1 bound to the 60S ribosomal subunit. Nat Struct Mol Biol. 2012; 19:1228–1233. [PubMed: 23142985]
41. Bradatsch B, et al. Structure of the pre-60S ribosomal subunit with nuclear export factor Arx1 bound at the exit tunnel. Nat Struct Mol Biol. 2012; 19:1234–1241. [PubMed: 23142978]
42. Valli R, et al. Different loss of material in recurrent chromosome 20 interstitial deletions in Shwachman-Diamond syndrome and in myeloid neoplasms. Mol Cytogenet. 2013; 6:56. [PubMed: 24330778]
43. Yokoyama T, et al. Structural insights into initial and intermediate steps of the ribosome-recycling process. EMBO J. 2012; 31:1836–1846. [PubMed: 22388519]
44. van Heel M, Harauz G, Orlova EV, Schmidt R, Schatz M. A new generation of the IMAGIC image processing system. J Struct Biol. 1996; 116:17–24. [PubMed: 8742718]
45. Bai XC, Fernandez IS, McMullan G, Scheres SH. Ribosome structures to near-atomic resolution from thirty thousand cryo-EM particles. eLife. 2013; 2:e00461. [PubMed: 23427024]
46. Tang G, et al. EMAN2: an extensible image processing suite for electron microscopy. J Struct Biol. 2007; 157:38–46. [PubMed: 16859925]
47. Mindell JA, Grigorieff N. Accurate determination of local defocus and specimen tilt in electron microscopy. J Struct Biol. 2003; 142:334–347. [PubMed: 12781660]
48. Scheres SH. A Bayesian view on cryo-EM structure determination. J Mol Biol. 2012; 415:406–418. [PubMed: 22100448]
49. Scheres SH. RELION: implementation of a Bayesian approach to cryo-EM structure determination. J Struct Biol. 2012; 180:519–530. [PubMed: 23000701]
50. Klaholz BP, Myasnikov AG, Van Heel M. Visualization of release factor 3 on the ribosome during termination of protein synthesis. Nature. 2004; 427:862–865. [PubMed: 14985767]
51. Penczek PA, Frank J, Spahn CM. A method of focused classification, based on the bootstrap 3D variance analysis, and its application to EF-G-dependent translocation. J Struct Biol. 2006; 154:184–194. [PubMed: 16520062]
52. Scheres SH, Chen S. Prevention of overfitting in cryo-EM structure determination. Nat Methods. 2012; 9:853–854. [PubMed: 22842542]

53. Chen S, et al. High-resolution noise substitution to measure overfitting and validate resolution in 3D structure determination by single particle electron cryomicroscopy. Ultramicroscopy. 2013; 135:24–35. [PubMed: 23872039]
54. Rosenthal PB, Henderson R. Optimal determination of particle orientation, absolute hand, and contrast loss in single-particle electron cryomicroscopy. J Mol Biol. 2003; 333:721–745. [PubMed: 14568533]
55. Larkin MA, et al. Clustal W and Clustal X version 2.0. Bioinformatics. 2007; 23:2947–2948. [PubMed: 17846036]
56. Jossinet F, Ludwig TE, Westhof E. Assemble: an interactive graphical tool to analyze and build RNA architectures at the 2D and 3D levels. Bioinformatics. 2010; 26:2057–2059. [PubMed: 20562414]
57. Emsley P, Lohkamp B, Scott WG, Cowtan K. Features and development of Coot. Acta Crystallogr D Biol Crystallogr. 2010; 66:486–501. [PubMed: 20383002]
58. Zhang Y. I-TASSER server for protein 3D structure prediction. BMC Bioinformatics. 2008; 9:40. [PubMed: 18215316]
59. Roy A, Kucukural A, Zhang Y. I-TASSER: a unified platform for automated protein structure and function prediction. Nat Protoc. 2010; 5:725–738. [PubMed: 20360767]
60. Pettersen EF, et al. UCSF Chimera: a visualization system for exploratory research and analysis. J Comput Chem. 2004; 25:1605–1612. [PubMed: 15264254]
61. Amunts A, et al. Structure of the yeast mitochondrial large ribosomal subunit. Science. 2014; 343:1485–1489. [PubMed: 24675956]
62. Humphrey W, Dalke A, Schulten K. VMD: visual molecular dynamics. J Mol Graph. 1996; 14:33–38. 27–28. [PubMed: 8744570]
63. Trabuco LG, Villa E, Mitra K, Frank J, Schulten K. Flexible fitting of atomic structures into electron microscopy maps using molecular dynamics. Structure. 2008; 16:673–683. [PubMed: 18462672]
64. Phillips JC, et al. Scalable molecular dynamics with NAMD. J Comput Chem. 2005; 26:1781–1802. [PubMed: 16222654]
65. Mackerell AD Jr, Feig M, Brooks CL III. Extending the treatment of backbone energetics in protein force fields: limitations of gas-phase quantum mechanics in reproducing protein conformational distributions in molecular dynamics simulations. J Comput Chem. 2004; 25:1400–1415. [PubMed: 15185334]
66. MacKerell AD Jr, Banavali N, Foloppe N. Development and current status of the CHARMM force field for nucleic acids. Biopolymers. 2000; 56:257–265. [PubMed: 11754339]
67. Chen VB, et al. MolProbity: all-atom structure validation for macromolecular crystallography. Acta Crystallogr D Biol Crystallogr. 2010; 66:12–21. [PubMed: 20057044]
68. Krissinel E, Henrick K. Inference of macromolecular assemblies from crystalline state. J Mol Biol. 2007; 372:774–797. [PubMed: 17681537]

Europe PMC Funders Author Manuscripts

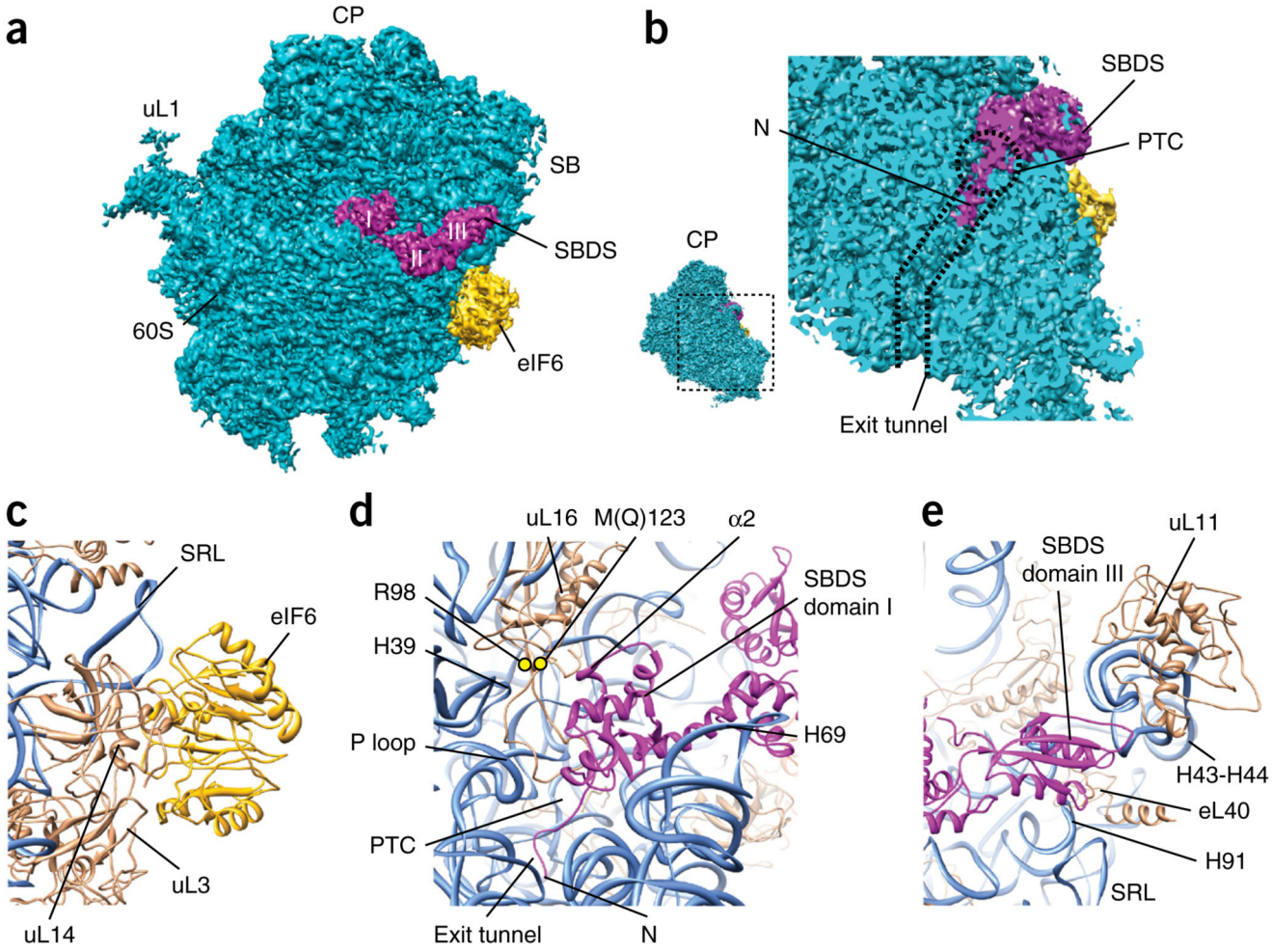

Figure 1.

SBDS shields the active sites of the 60S subunit. (**a**,**b**) Crown view (**a**) and transverse section (**b**) of the cryo-EM map of the 60S–eIF6–SBDS complex, filtered to 4 Å. The 60S ribosomal subunit is shown in cyan, eIF6 in yellow and SBDS in magenta. CP, central protuberance; SB, stalk base; PTC, peptidyl transferase center; N, N terminus. (**c**–**e**) Atomic models of the interface between the 60S ribosomal subunit and eIF6 (**c**), SBDS domain I (**d**) and SBDS domain III (**e**). 26S rRNA is shown in blue, ribosomal proteins in beige, eIF6 in yellow and SBDS in magenta. Residues R98 and M123 (Q123 in humans) of human uL16 that are mutated in T-ALL13, are indicated. SRL, sarcin-ricin loop.

Europe PMC Funders Author Manuscripts

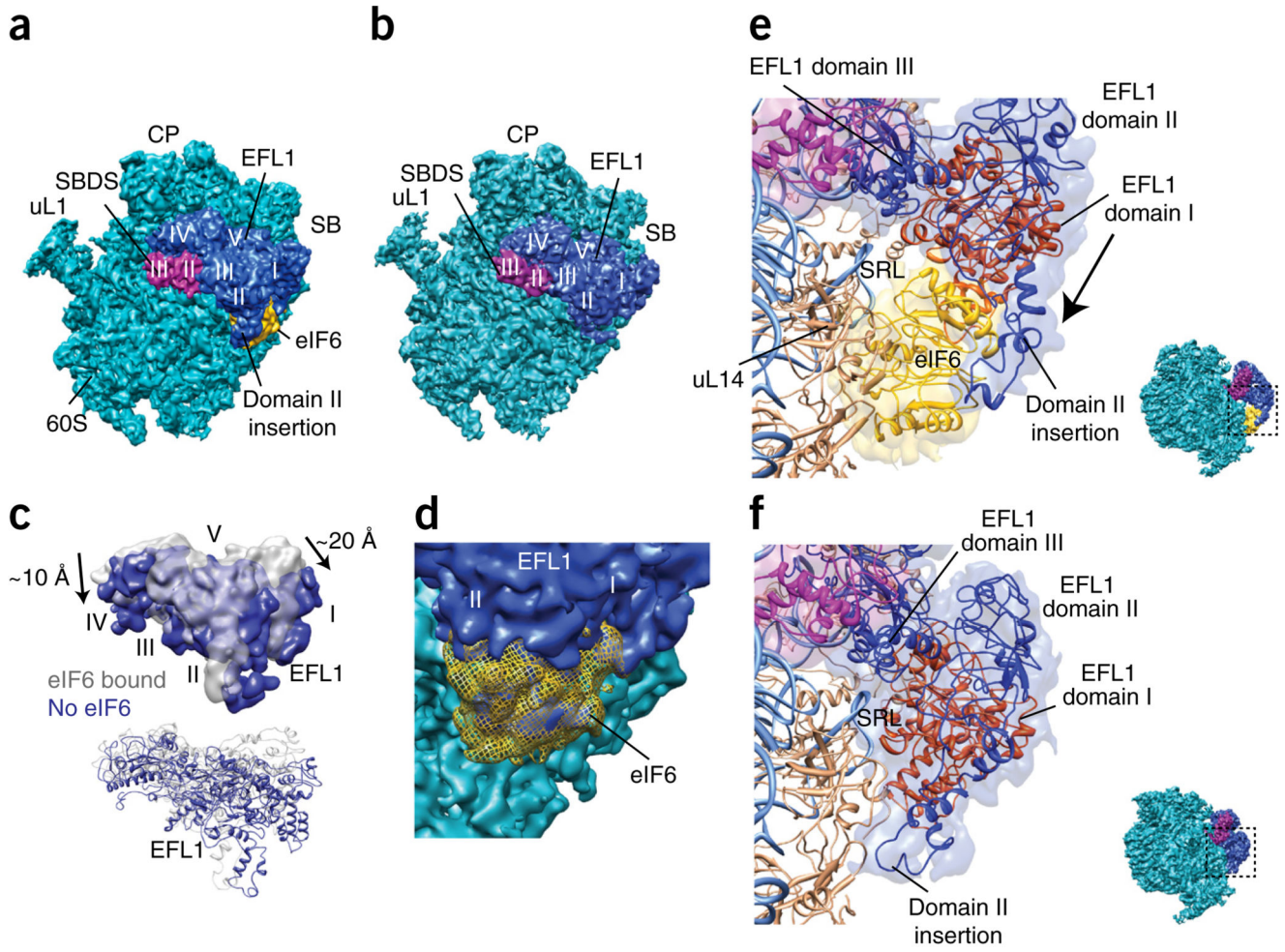

Figure 2.

EFL1 and eIF6 compete for an overlapping binding site. (**a**,**b**) Crown views of the cryo-EM maps of the 60S–eIF6–SBDS–EFL1 (**a**) and 60S–SBDS–EFL1 (**b**) complexes, filtered to 6 Å. EFL1 is in dark blue. CP, central protuberance; SB, stalk base. (**c**) Superposition of the cryo-EM densities, filtered to 6 Å (top) or atomic models (bottom) of EFL1 in the presence (gray) or absence (dark blue) of eIF6. (**d**) The volume previously occupied by eIF6, highlighted in yellow mesh in the 60S–SBDS–EFL1 cryo-EM map. (**e**,**f**) Atomic models of the 60S–SBDS–EFL1 complex with (**e**) or without (**f**) eIF6. 26S rRNA is in blue, ribosomal proteins in beige, SBDS in magenta, EFL1 domain I in orange, EFL1 domains II–V in dark blue and eIF6 in yellow.

Europe PMC Funders Author Manuscripts

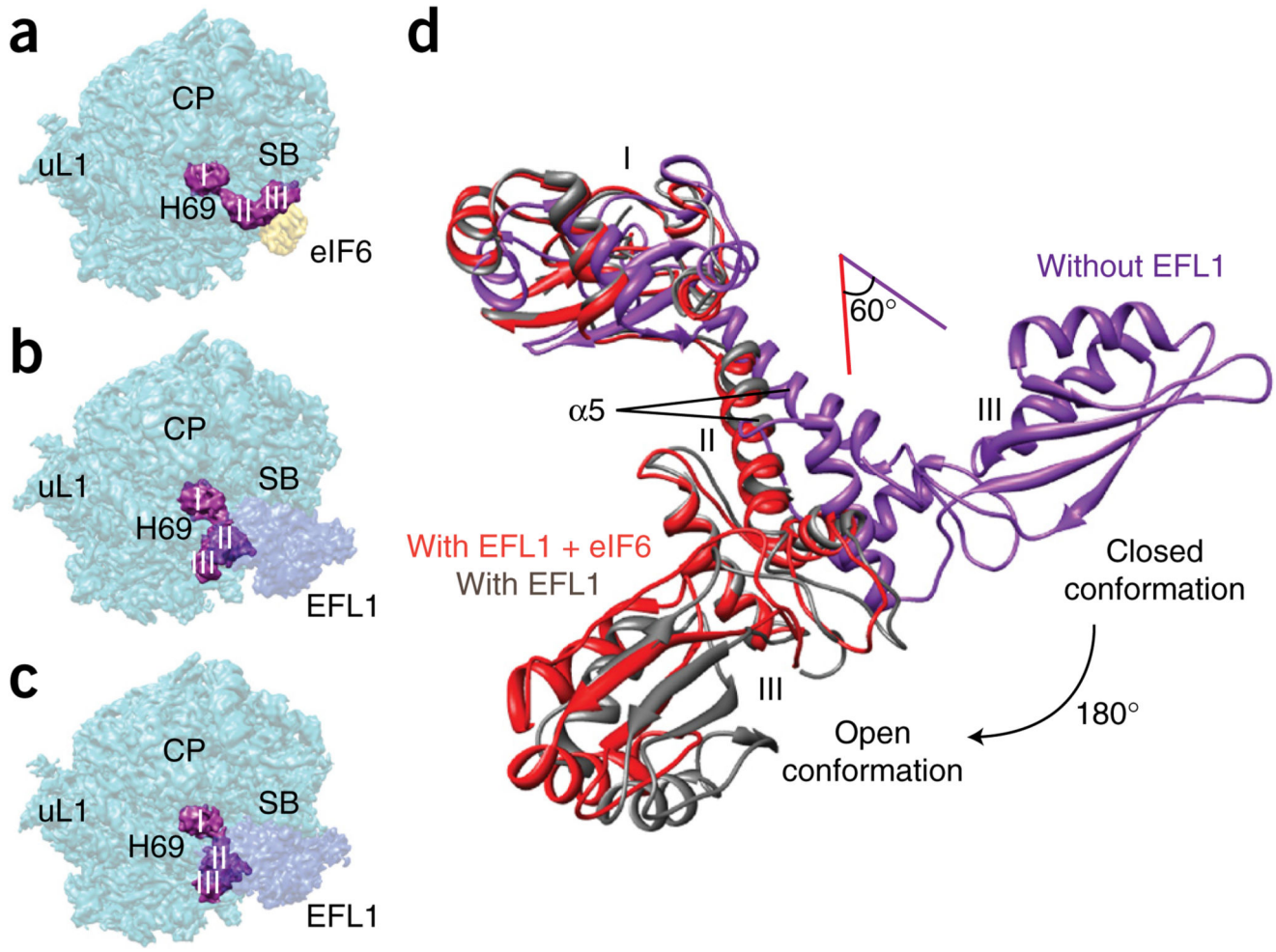

Figure 3.

Rotational displacement of SBDS upon EFL1 binding. (**a**–**c**) Top views of 60S–eIF6–SBDS (**a**), 60S–eIF6–SBDS–EFL1 (**b**) and 60S–SBDS–EFL1 (**c**) complexes. SBDS is shown in magenta, the 60S subunit in cyan, eIF6 in yellow and EFL1 in dark blue. For clarity, 60S, eIF6 and EFL1 densities are shown in transparency. The uL1 protein stalk (uL1), central protuberance (CP) and P-stalk base (SB) are indicated. (**d**) Superposition of the SBDS structures from the 60S–eIF6–SBDS (purple), 60S–eIF6-SBDS–EFL1 (red) and 60S–SBDS–EFL1 (black) complexes. SBDS helix α5 is indicated.

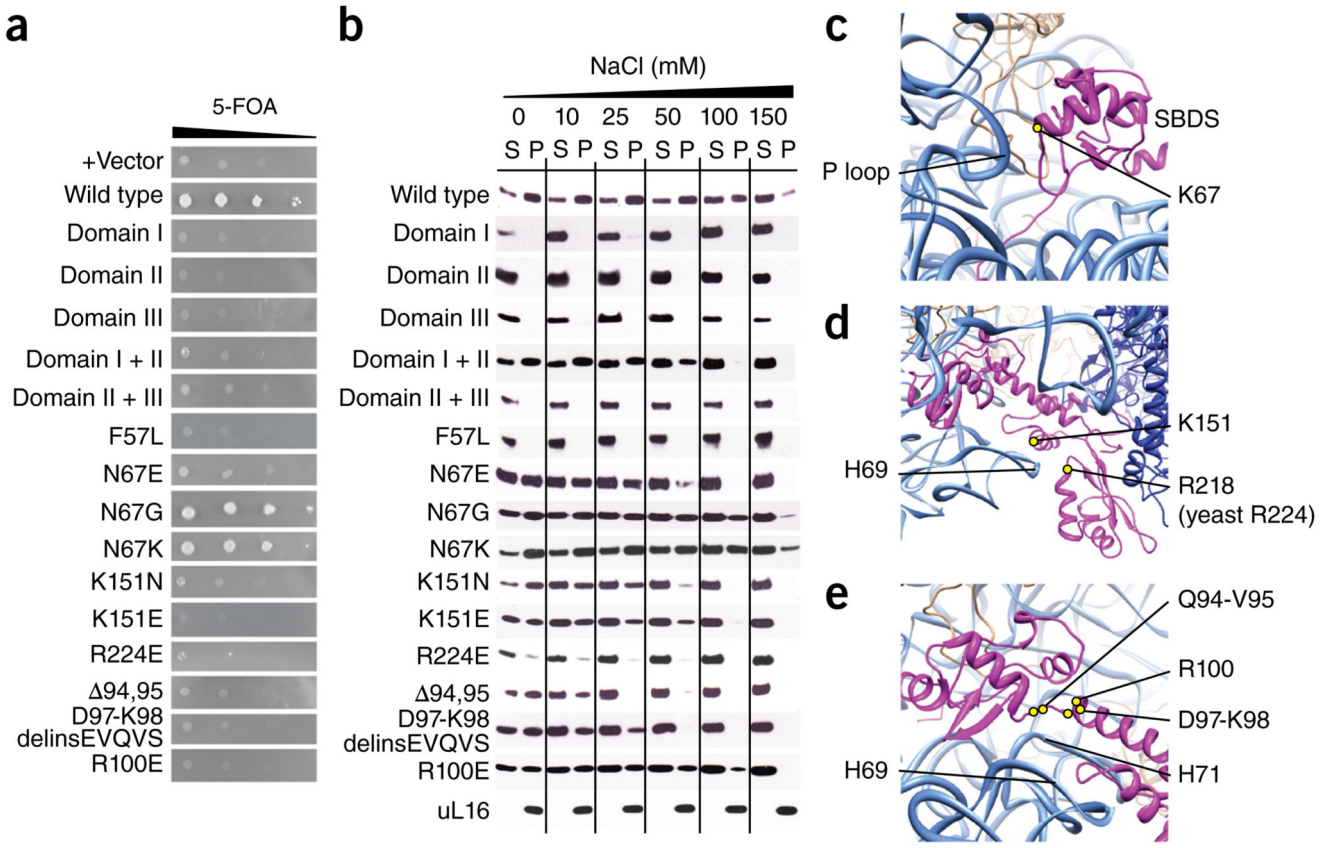

Figure 4.

Disease-related SBDS variants disrupt critical interactions with the 60S rRNA. (**a**) Complementation of *sdo1*Δ cells by disease-related *SDO1* variant alleles. Ten-fold serial dilutions (from left to right) of the indicated strains are shown. 5-FOA, 5-fluoroorotic acid. (**b**) Impaired 60S-subunit binding of disease-related Sdo1 variants *in vivo*. FLAG-tagged Sdo1 was visualized in the supernatant (S) and pellet (P), and uL16 was visualized in the pellet across the indicated range of NaCl concentrations by immunoblotting. (**c**–**e**) Mapping disease-related SBDS residues in the 60S–eIF6–SBDS–EFL1 atomic model including K67 (**c**), K151 and R218 (**d**) and Q94-V95 and D97-K98 (**e**).

Europe PMC Funders Author Manuscripts

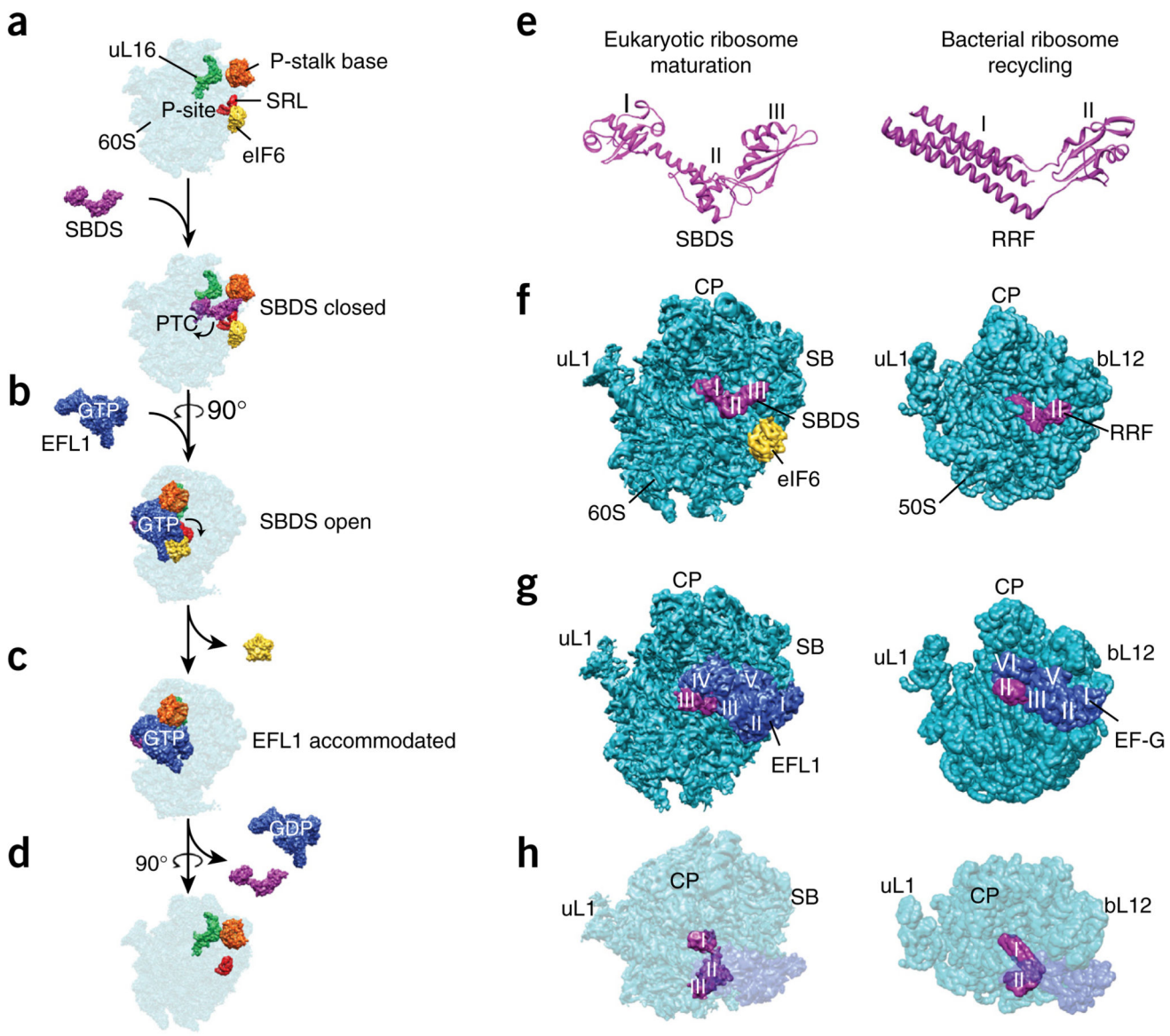

Figure 5.

Mechanism of eIF6 release by SBDS and EFL1. (**a**) SBDS (closed state) is recruited to a late cytoplasmic eIF6-loaded pre-60S subunit after P-stalk base assembly and uL16 recruitment. (**b**) EFL1–GTP (or EF-2–GTP in archaea) binds directly to SBDS and eIF6 in the GTPase center, thus promoting rotational displacement (180°) of SBDS domain III away from the P-stalk base toward helix 69 (open state), which is stabilized by SBDS residues K151 and R218. (**c**) GTP-bound EFL1 in the accommodated state competes with eIF6 for an overlapping binding site on the 60S subunit, thus promoting eIF6 displacement. (**d**) Interaction of EFL1–GTP with the SRL promotes GTP hydrolysis, thus triggering a conformational switch in EFL1 that promotes a low-affinity ribosome binding state. SBDS and EFL1–GDP dissociate from the 60S subunit. (**e**–**h**) Eukaryotic ribosome maturation is structurally reminiscent of prokaryotic ribosome recycling. Atomic models of human SBDS

(left) from the 60S–eIF6–SBDS complex, ribosome-recycling factor (RRF) from *Thermus thermophilus* (right) (PDB 3J0D)43 (**e**) and density maps of SBDS (left) and RRF (right) bound to the large ribosomal subunit in the absence (**f**) or presence (**g**,**h**) of EFL1 (left) or EF-G (right). The 60S subunit (60S, left; 50S, right) is in cyan, SBDS (domains I–III) and RRF (I and II) in purple, EFL1 (I–V) and EF-G (I–V) in dark blue, eIF6 in yellow. uL1, uL1 protein stalk; CP, central protuberance; SB, P-stalk base; bL12, bL12 protein stalk. Density maps for the 50S–RRF and 50S–RRF–EFG complexes were generated from PDB 3J0D43 and PDB 2RDO33 with IMAGIC-V44.

Europe PMC Funders Author Manuscripts